Proceedings of the ASME Turbo Expo 2026
Turbomachinery Technical Conference and Exposition
GT2026
June 15–19, 2026, Milan, Italy

GT2026-178157

DESIGN AND OPTIMIZATION OF AN OPEN ROTOR STAGE

John L. Gillespie[1,*], Kristopher C. Pierson[1], Matthew J. Ha[2], Mark G. Turner[1]

[1]NASA Glenn Research Center, Brook Park, Ohio
[2]HX5, LLC, NASA Glenn Research Center, Brook Park, Ohio

ABSTRACT

Open rotor propulsors enable greatly increased effective bypass ratios over current aircraft engines, resulting in significantly improved efficiencies. One of the most promising of these geometries is the "open fan", which consists of a single rotor followed by a single stator. This configuration will be referred to as an "open rotor stage" for design work at NASA. In this work we consider the multidisciplinary design and optimization of an open rotor stage using a variety of 2D and 3D techniques. The 2D aerodynamic techniques used for design include a 2D Trefftz plane method, axisymmetric throughflow, and quasi-3D blade-to-blade CFD. Aerodynamic performance is prioritized, while structural requirements are met and some acoustic considerations are included. Between the rotor, stator, and hub profiles, a total of 101 design variables are used. Differences in the process of designing an open rotor stage vs. designing other high-speed propellers are also discussed. The current design, the NASA Optimized Propulsor for Efficiency and Noise (N-OPEN-1), achieves 84.7% net efficiency as predicted by 3D CFD, with further improvements expected to be possible. This design makes effective use of a slower rotor and a less tip-loaded work distribution than typical single-rotation propellers, allowing the stator to produce 14.8% of the thrust. Laminar flow on the blades was responsible for a 1.7% efficiency benefit and warrants further study.

Keywords: open rotor, multidisciplinary optimization, turbomachinery

NOMENCLATURE

Roman letters

A	hub contour height [m]
b	hub contour location [m]
c	chord [m]
E	elastic modulus [GPa]
$\dot{E}_a$	Streamwise KE deposition rate [kW]
$\dot{E}_v$	Transverse KE deposition rate [kW]
$\dot{E}_p$	Pressure-work deposition rate [kW]
f	objective function [-]
FS	Factor of Safety [-]
h	altitude [m]
Ma	Mach number [-]
P	pressure [Pa]
r	radius [m]
t	thickness [m]
T	temperature [K]
uvw	Cartesian velocity components [m/s]
V	velocity [m/s]
w	hub contour width [m]
$\boldsymbol{x}$	design variable
xyz	Cartesian coordinates [m]

Greek letters

α	angle of attack [°]
β	blade relative angle [°]
η_{NET}	net efficiency [%]
η_{prop}	propulsive efficiency [%]
η_{trans}	transfer efficiency [%]
σ	stress [MPa]
ρ	density [kg/m^3]
$\overline{\omega}$	loss coefficient [-]
Ω	rotational speed [rad/s]
Φ	dissipation rate [kW]

Superscripts and subscripts

1	upstream
2	downstream
i	per section
∞	free stream value

*Corresponding author: john.l.gillespie@nasa.gov

1. INTRODUCTION

Open rotor propulsors can greatly reduce fuel consumption relative to existing ducted turbofans. Increasing bypass ratio of a turbofan increases propulsive efficiency: it is inherently more efficient to accelerate a large quantity of air by a small amount than to generate the same amount of thrust by accelerating a smaller quantity of air by a large amount. This has driven continuous increases in fan diameter and decreases in fan pressure ratio for state-of-the-art turbofans. The nacelle of a ducted turbofan must get larger along with the fan diameter, increasing weight and drag. Therefore, the maximum bypass ratio of a ducted fan is limited. An open rotor, or propeller, does not require an external nacelle, enabling much greater effective bypass ratio. However, efficient design of an open rotor must contend with other challenges, most notably shock losses associated with the high relative Mach number at the tip as well as secondary losses associated with the tip vortices and residual swirl produced by the rotor. Acoustic performance is another large challenge: the exposed rotor generates significant noise, which may make meeting future noise targets difficult.

As a result, there were significant research efforts beginning in the 1970s and 1980s into the design of open rotor geometries that can overcome these challenges with the NASA Advanced Turboprop Program (ATP) [1–4]. As part of this program, Hamilton Standard designed a series of "propfans" intended to operate up to cruise Mach numbers of 0.8. These were single rotors (numbered SR-1 through SR-7, for "Single Rotation") and were designed with thin airfoil sections, swept-back blades, and more blades (8 or 10) than are typical for a lower-speed turboprop [5]. The design process for these rotors modeled airfoil sections nearest to the hub (specifically, where the spacing between adjacent blades was shorter than 1 chord length) using conventional turbofan aerodynamics, sections further away from the hub using turboprop design methodology, and sections near the tip as swept wings [5, 6]. The single-rotation models were tested in the NASA Lewis Research Center (now NASA Glenn Research Center) 8x6 ft supersonic wind tunnel, and SR-3 with 45° tip sweep was shown to have a net efficiency 2.0% higher than the 30° swept SR-1 and 2.4% higher than the unswept SR-2, as well as better acoustic performance [7]. This was attributed to the newly-developed acoustic prediction methodology that was used to tailor the sweep of SR-3 [5]. SR-5 and SR-6 were designed to operate with lower tip speeds intended to reduce noise, but encountered aeromechanical issues preventing complete testing [8, 9]. The final single-rotation rotor designed as part of the ATP program, SR-7A achieved a net efficiency of 79.3% when tested in the 8x6 ft wind tunnel [10]. A full-scale version of this rotor, SR-7L, was additionally tested at its rated power (but zero free stream velocity) at the Wright Aeronautical Laboratory [11], and at the design cruise Mach number (but at a reduced power) in the ONERA S1-MA Large Atmospheric Wind Tunnel [12].

A major disadvantage of single-rotation propellers is that they leave considerable residual swirl in the slipstream; the kinetic energy of this swirl is wasted power. This swirl also can have adverse effects on the airframe; for example, it was found that the swirl from the propeller could contribute significantly to the cruise drag of the aircraft [1]. By using counter-rotating propellers, it is possible to remove this swirl component of the slipstream, increasing the overall system efficiency. Multiple industry efforts in the 1980s, partially supported by the NASA ATP program, led to flight tests of counter-rotating propfans. Hamilton Standard designed and tested the CRP-X1 counter-rotating propfan in the UTRC Large Subsonic Wind Tunnel [14]. This work would eventually lead to the development of the Allison/Pratt &

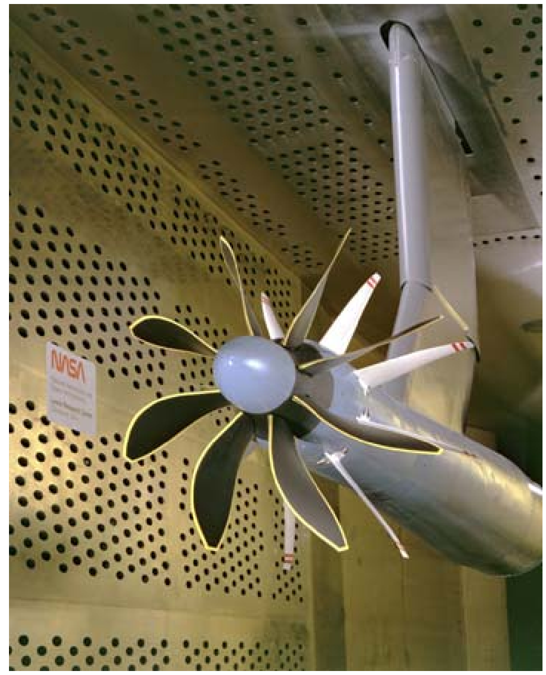

FIGURE 1: Single Rotation (SR-7A) rotor with swirl recovery vanes installed in NASA Glenn 8x6 Supersonic Wind Tunnel [13].

Whitney 578-DX geared propfan, which was flight tested on a McDonnell Douglas MD-80 aircraft [15]. Concurrently, General Electric developed a gearless counter-rotating system, the Unducted Fan [16], which utilized a counter-rotating power turbine in order to drive the two rotors. A series of tests in the GE anechoic freejet facility, NASA 8x6 wind tunnel, and the Boeing Transonic Wind Tunnel were performed, ultimately culminating in a flight test on a Boeing 727 airframe [17, 18]. Both Hamilton Standard and GE efforts demonstrated designs exceeding 85% net efficiency during wind tunnel testing [14, 17], outperforming single-rotation systems by more than 5%. However, the interaction noise between the two rotors was a problem, and falling fuel prices decreased the demand for a major engine architecture change [4].

Recently there has been revived interest in open rotor technologies. A partnership between GE, NASA, and the FAA resulted in tests of a new counter-rotating design in the NASA 8x6 and 9x15 wind tunnels. Leveraging modern CFD and aeroacoustic techniques, the new blades designed by GE significantly reduced noise (with an expected 15-17 EPNdB margin to FAA Stage 4 requirements) while also improving aerodynamic efficiency above the historical designs [19]. Additionally, many authors have made recent contributions to computational modeling of counter-rotating open rotor aerodynamics and acoustics [20–23].

However, counter-rotating propellers still have the disadvantage of increased mechanical complexity, as well as a second set of fundamental blade passing tones from the second rotor. As a result, there has been interest in geometries that combine a single rotor with a set of stator vanes intended to remove most of the swirl left by the rotor. By replacing the second rotor with a stator, the mechanical complexity is reduced and the second rotor blade

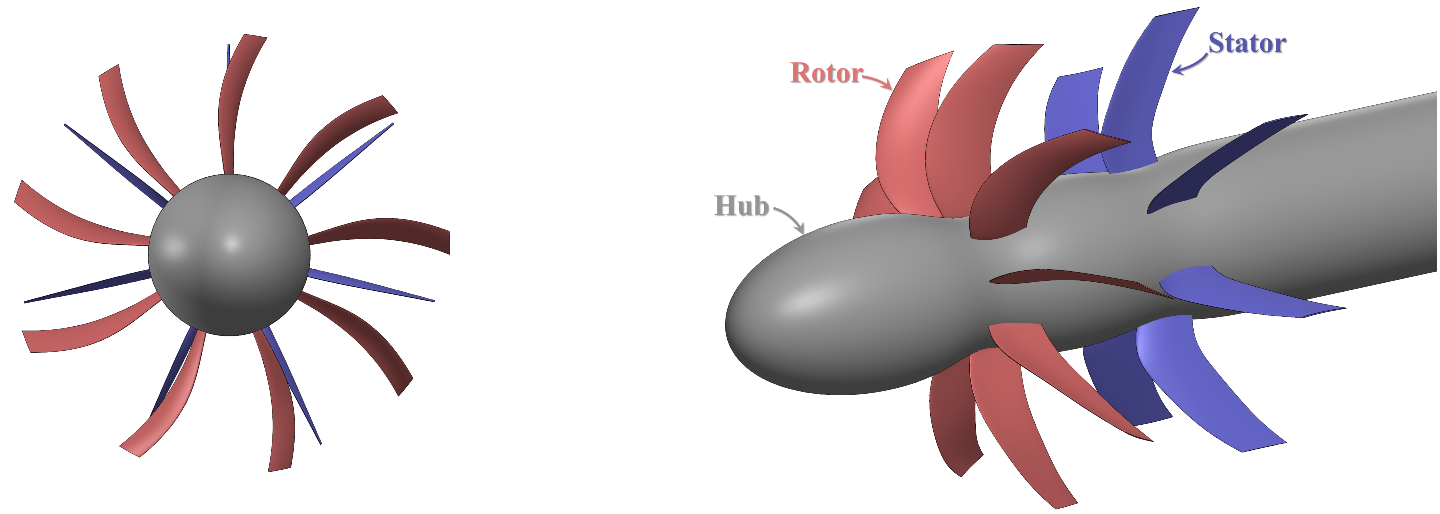

(a) (b)

FIGURE 2: NASA Optimized Propulsor for Efficiency and Noise (N-OPEN-1), an open rotor stage geometry consisting of a single 9-blade rotor followed by a single 7-vane stator on a contoured hub. a) forward-looking-aft view, b) isometric view.

passing tones are eliminated, while comparable aerodynamic performance to a counter-rotating design should be achievable. This bears a close resemblance to the single-stage fan used in typical high-bypass turbofans, and has been referred to as an "open fan". The CFM RISE program proposes an Open Fan architecture to propel a single aisle aircraft at Mach 0.80 [24]. In this work, we will refer to a combined rotor + stator geometry as an open rotor stage to avoid confusion with this particular CFM design. Some early work on a open rotor + stator concept involved retrofitting the SR-7A propeller with a set of "swirl recovery vanes" [13], which demonstrated a small benefit in efficiency over the isolated propeller (at design conditions). This open rotor + stator test is shown in Fig. 1.

The process of designing an efficient open rotor stage is not simply the process of designing an efficient propeller and retrofitting it with a set of swirl recovery vanes. In particular, the choices of advance ratio and work distribution that are optimal for a single isolated propeller are far from optimal for a fan stage consisting of a rotor plus a stator. While retrofitted swirl recovery vanes can enhance performance (relative to a single isolated rotor), significant further performance can be achieved by considering the stage as a single unit. There are two principle advantages of this integrated approach.

First, the rotor of the fan stage can be designed to operate at a higher advance ratio (i.e., lower rotational speed) than would be optimal for an isolated propeller. This is because the swirl losses of the propeller increase with advance ratio due to the increased disk loading required to maintain the required work input. This is in contrast to airfoil profile losses (in particular shock losses), which will generally decrease with advance ratio: the balancing point between these losses will determine the best advance ratio to design for the rotor. For an open rotor stage, the stator recovers the majority of the energy associated with this swirl. As a result, the balance point shifts towards higher advance ratio, resulting in reduced shock losses on the rotor.

Secondly, the work distribution from hub to tip that is optimal for an open rotor stage is not the same as for an isolated propeller. Much work has been performed to determine the best work distribution for a propeller, and the optimum has been found for a wide variety of conditions [25–28]. Notably, for a many-bladed isolated propeller, the circulation must decrease considerably near the hub. This is necessary because otherwise the axisymmetric component of the swirl kinetic energy would rise to an unacceptable level. However, an unavoidable consequence of this is that the work performed by the propeller is very nonuniform with radius, with the portion between 50% and 85% span doing more work, and the portion of the span closest to the hub doing very little work. This comes with a decrease in isentropic efficiency, because this region represents a significant contribution to wetted area (as well as high blockage near the hub) while not contributing much useful work. The resulting non-uniformities in axial velocity, as well as the strong tip vortices, also contribute to a loss of propulsive efficiency. Despite these factors, this is still the optimal balance of losses for an isolated rotor.

In contrast, the stator of an open rotor stage removes the majority of axisymmetric swirl leaving the rotor. As a result, the open rotor stage can run efficiently with a much more uniform circulation distribution. The optimal distribution for an open rotor stage is close to a free-vortex distribution for a ducted fan, only with a careful reduction near the tip to reduce tip vortex losses. This resembles the solutions for a counter-rotating propeller demonstrated by Theodorsen [27]. This updated distribution of circulation allows blade loading to be kept more consistent along the blade span, reducing isentropic losses.

The stationary blade row following a fan in a turbofan engine is often referred to as an Outlet Guide Vane (OGV) or Exit Guide Vane (EGV), and that terminology has been used for the open stator in some references. In this work, it is referred to as a stator so the concept that this is a stage is reinforced.

In this paper, we explore the preliminary design and optimization of an open rotor stage, incorporating both aerodynamic and structural requirements. The open rotor geometry optimized as part of this paper, the NASA Optimized Propulsor for Efficiency and Noise (N-OPEN-1), is shown in Fig. 2. This type of design attempts to produce high efficiency, comparable to a counter-rotating design, while requiring a similar number of moving parts as a single rotor. Overall, the methodology resembles that presented by Smith [29] for counter-rotating open rotors, with some modifications for using a stator instead of an aft rotor. However, we also take advantage of nearly 40 years of improvements in numerical methods and computational resources. In particular, methods that once were considered computationally demanding (e.g., 2D blade-to-blade CFD) can now be executed massively in parallel, enabling detailed multidisciplinary optimizations. Finite element analysis for verifying structural integrity can also be rapidly executed. The three main 2D projections of the flow (onto a meridional plane for throughflow analysis, onto an axisymmetric streamsurface for blade-to-blade CFD, and onto the Trefftz plane to look at secondary flows) are all considered and provide different critical information to the system design. By combining these techniques with appropriate optimization algorithms, a design that performs well aerodynamically while meeting structural requirements is obtained. Performance is then examined using 3D CFD.

2. DESIGN AND ANALYSIS METHODOLOGY

In order to create an effective open rotor stage design, multiple disciplines must be considered, including aerodynamics, structures, and acoustics. While 3D CFD can capture all of the relevant aerodynamic effects, it can be computationally expensive, especially in the context of optimization. Optimizing the full set of design variables considered within this paper (101) using only 3D CFD would be challenging even in 2025, though advances in adjoint methods and high performance computing may soon make this practical. As a result, it is useful to analyze the aerodynamic performance using two-dimensional tools which can also allow for improved understanding of the design space. Structures must also be considered; the blade thickness is driven by strength requirements. Acoustics are also of primary importance to open rotors. For this preliminary design, only key principles for acoustics were utilized, and no aeroacoustic analysis was included in the optimization loop.

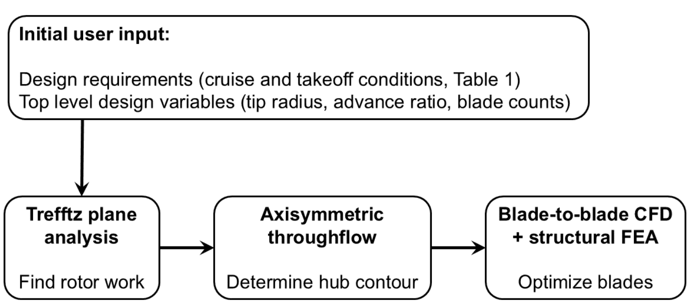

FIGURE 3: Design process overview.

Figure 3 is a flowchart summarizing the design process utilizing 2D aerodynamic methods. Each of the 2D methods feeds information into the next analysis. First, the distribution of swirl in a Trefftz plane downstream of the rotor (which is directly tied to the work done by the rotor) is considered. Next, this swirl distribution is used with an axisymmetric throughflow solver to determine an appropriate hub contour profile. Finally, the streamsurfaces from the throughflow analysis are mapped to the $m' - \theta$ plane where they are used for a blade-to-blade analysis. This blade-to-blade analysis enables the optimization of airfoil sections, while accounting for boundary layer transition, and is run simultaneously with finite element analysis to evaluate structural performance.

	Ma_∞	P_∞	T_∞	Thrust	α
Cruise	0.785	23.9 kPa	218.9 K	18.3 kN	0°
Climb-out	0.250	101.3 kPa	303.1 K	109.3 kN	12°
Takeoff	0.250	101.3 kPa	303.1 K	109.3 kN	0°

TABLE 1: Design requirements for N-OPEN-1.

For this design, a "vision vehicle" narrowbody aircraft was considered, broadly corresponding to a Boeing 737 or Airbus A320. Cruise was set to a Mach number of 0.785 at 10,668 m (35,000 ft). The cruise thrust requirement was chosen to be 18.3 kN, anticipating reductions in airframe weight and drag, as well as compounding benefits from the improved efficiency of the open rotor design reducing the required fuel load. A full list of design requirements is included in Table 1. Note that the angle-of-attack is relative to trim at cruise (i.e., cruise α is set to 0° by definition for the purpose of this analysis).

The rotor tip radius was chosen to be 2.668 m. With a hub-to-tip ratio of 0.35 (hub radius 0.934 m) and an assumed net efficiency of about 80%, this results in a power loading of 271 kW m^{-2}. This is comparable to SR-3, which had a power loading at peak efficiency of 247 kW m^{-2} at $\mathrm{Ma}_\infty = 0.75$ and 300 kW m^{-2} at $\mathrm{Ma}_\infty = 0.80$ [7]. The design advance ratio was chosen to be 4.71, resulting in a helical tip Mach number of 0.95 at cruise. Nine (9) rotor blades and 7 stator vanes were used, avoiding common factors that may lead to worsened noise or aeromechanics response.

Table 2 provides an overview of which design variables were active during which optimization phase. The blade geometry is parameterized using T-Blade3 (formerly called 3DBGB) [30, 31]. A total of 47 adjustable parameters were considered for each blade row, controlling the airfoils sections as well as their stacking (sweep and lean). Leading and trailing edge metal angles were controlled at 5 spanwise locations, and a total of 18 camber control points (6 B-spline points at each of 3 spanwise sections) were used. Airfoil thickness parameterization used a modified NACA four-digit distribution [32], with design parameters for the chord length, maximum thickness, max thickness location, and leading edge radius applied at 3 spanwise sections. Stacking was controlled through 5 spanwise values for sweep and 2 free values for lean. Including both blade rows, the 6 hub contouring parameters, and rotor circulation, a total of 101 design parameters were considered.

The aerodynamic effect of lean is not possible to capture properly with these methods, so it is not an active design variable

Design Variable		Trefftz Plane	Axisymmetric Throughflow	Blade-to-Blade
Circulation $\Delta\Gamma$	$\times 1$	✓		
Hub contour b_i	$\times 2$		✓	
Hub contour A_i	$\times 2$		✓	
Hub contour w_i	$\times 2$		✓	
Rotor β_1	$\times 5$			✓
Rotor β_2	$\times 5$			✓
Rotor camber	$\times 18$			✓
Rotor c	$\times 3$			✓
Rotor t_{max}	$\times 3$			✓
Rotor $x(t_{max})$	$\times 3$			✓
Rotor r_{LE}	$\times 3$			✓
Rotor sweep	$\times 5$			✓
Rotor lean	$\times 2$			
Stator β_1	$\times 5$			✓
Stator β_2	$\times 5$			✓
Stator camber	$\times 18$			✓
Stator c	$\times 3$			✓
Stator t_{max}	$\times 3$			✓
Stator $x(t_{max})$	$\times 3$			✓
Stator r_{LE}	$\times 3$			✓
Stator sweep	$\times 5$			✓
Stator lean	$\times 2$			

TABLE 2: Active design variables for each optimization phase.

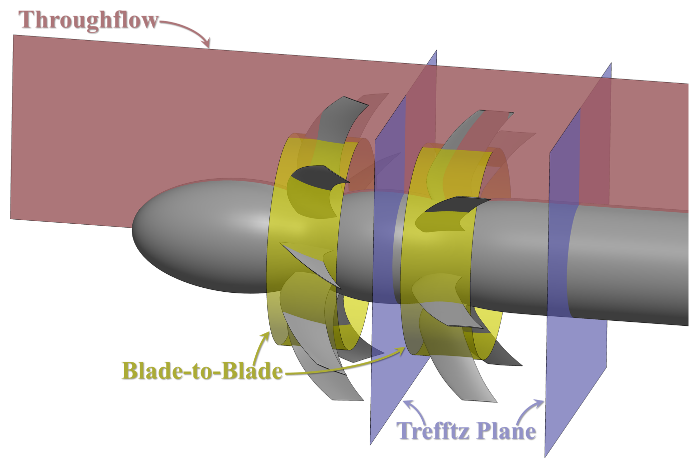

FIGURE 4: Surface types for the 2D aerodynamic methods used to design N-OPEN-1 (axisymmetric throughflow, blade-to-blade, and Trefftz plane analysis).

at any phase in the process. Lean (also called dihedral) affects the radial equilibrium of the flow by introducing a radial component to the force from the blades [33, 34]. Lean also affects the acoustic performance via spanwise phasing effects [21]. A complete analysis of these effects depends on 3D CFD, and true optimization of lean will require optimizing in 3D. However, lean is also of significant influence structurally because it affects the distribution of mass for the centrifugal loading, and it is desirable to account for this effect even during the 2D airfoil optimization. Therefore, an exploratory study of the structural influence of lean was carried out on an earlier rotor design, and the values obtained in that study were applied throughout the optimization process.

2.1. 2D Aerodynamics

Figure 4 shows the surfaces corresponding to each of the three two-dimensional aerodynamic methods used in the current work. In addition to enabling more efficient optimization, these 2D tools can provide physical insight into the flow that is difficult to obtain from 3D methods. For example, consider a case where shortening the blade chord at 25% span increases net efficiency. There are several possible explanations: the shorter chord could have improved the blade section geometry, reducing viscous losses. Or, it could have changed the exit deviation, aligning the work profile closer to the theoretical optimum. It is even possible that the improvement could be due to an interaction with the hub, as the maximum thickness location will have shifted axially relative to the hub endwall contouring. Each of these effects would influence a different 2D tool. By working with these tools, the effects of different design decisions can be more clearly observed, enhancing understanding.

2.1.1. 2D Trefftz plane analysis A noteworthy challenge of open rotor design is the strong influence of the tip vortices. While tip flows are important for ducted turbofans as well, their influence is largely confined to the immediate vicinity of the tip, and their effect is felt mostly as leakage losses and other secondary losses in the tip region. In contrast, the tip vortices of an open rotor (with no duct and a relatively low blade count) lead to highly three-dimensional flows across much of the blade span. The effect is physically much more analogous to the tip vortices of fixed-wing aircraft than the tip flows of ducted fans. The tip vortex alters the flow incidence along much of the span, resulting in a reduction in lift and a corresponding reduction in thrust. Additionally, the vortex carries away a non-negligible amount of kinetic energy, reducing efficiency. These two effects correspond to the reduction in lift for a finite wing and the generation of induced drag.

Much theoretical analysis has been performed to determine the optimal distribution of circulation (and corresponding distribution of work) behind a propeller. This includes early work by Goldstein [26] on lightly-loaded single propellers, and by Theodorsen [27] who extended Goldstein's work to heavily-loaded and dual counter-rotating propellers. These models solve for the flow behind a rigidly rotating helical wake (determined to be optimal in terms of losses) of infinitesimal thickness. Further progress was obtained once these models could be practically run on computers. Ribner and Foster [28] directly revisited Theodorsen's models and obtained further results, while Hanson [35] implemented a compressible lifting surface model capable of more accurately describing blade geometry.

The approach taken in this work to model tip effects is similar to that described by Smith [29], where a secondary flow is superimposed upon the axisymmetric primary flow. A prescribed swirl angle profile is applied along the trailing edge of each blade, which will be associated with a shed vortex sheet of infinitesimal thickness. The vorticity between the blades is also known to be zero (the inlet flow is irrotational). With appropriate boundary conditions applied at the hub surface and in

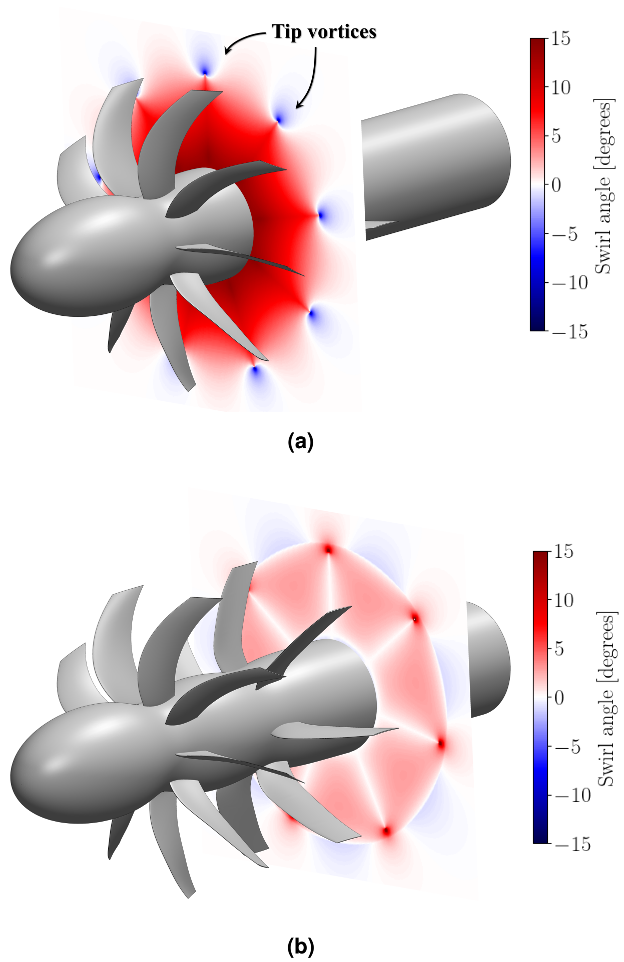

FIGURE 5: Swirl predicted by Trefftz plane analysis. a) downstream of rotor and upstream of stator, b) downstream of stator.

the far-field, a streamfunction for the flow throughout the Trefftz plane can be numerically solved for. From this streamfunction, the local flow velocities can also be estimated. Losses are then estimated by integrating the swirl kinetic energy throughout this Trefftz plane. Predictions for the Trefftz plane downstream of the stator are obtained similarly. The one difference is that a nonzero inlet vorticity (obtained from the circumferential average of the rotor flow) is used instead of an irrotational inlet. The full tip loss model is coupled with an actuator disk model in order to capture the streamtube contraction and the overall propulsive efficiency.

Importantly, this model can analyze non-optimal circulation distributions (in terms of tip vortex losses). This is necessary because sometimes the flow angles must be altered in order to accommodate realistic effects that are not accounted for by Theodorsen's model. For example, in the present work, a reduction in turning (relative to the theoretical optimum) on the innermost 25% of the rotor span was applied in order to avoid separated flow at the hub. This results in increased loss due to secondary kinetic energy, but is compensated for by the reduced viscous losses resulting from avoiding separation.

The method may also be modified to make predictions about off-design conditions. This is done by prescribing a new swirl distribution on the vortex sheets (derived from the design distribution, modified by an altered blade stagger and rotational speed, assuming deviation remains nearly constant) and re-running the analysis. By holding incidence at a particular mid-span radius constant (by selecting the new blade stagger as a function of the new rotor speed), a trend of thrust vs. rotor speed can be determined. This is useful for exploring takeoff and climb performance, and was used to determine the rotational speed required to meet a target takeoff thrust which is the structurally limiting case in the current work.

The application of this simple technique proved to be effective for preliminary design prior to 3D CFD. An early open rotor stage design was predicted to produce a thrust of 18.3 kN when tip effects were neglected, but only 12.3 kN after the tip vortex was accounted for. 3D CFD results showed a thrust of 12.5 kN, giving confidence that the tip model was sufficient to enable preliminary design tasks for additional designs. It should be noted that this 33% reduction in thrust does not correspond to a 33% reduction in efficiency, as the torque (and thus the input power) is also reduced by the tip vortices. When this is accounted for, tip losses result in an efficiency drop of between 5% and 10%, depending on the design.

The swirl distributions within the Trefftz planes downstream of the rotor and downstream of the stator for N-OPEN-1 are shown in Fig. 5. We see that the stator removes the majority of the swirl produced by the rotor, but some remains between each of the blades. It also generates its own set of tip vortices, similar in strength to those of the rotor. In total, the simple Trefftz plane model predicts that the rotor converts 22.8% of its input power into the swirl kinetic energy (19.6% of which is axisymmetric, and 3.19% of which is tip vortices). The stator is predicted to recover the majority of this energy, leaving only 2.97% as swirl kinetic energy (0.89% axisymmetric and 2.07% due the tip vortices). This will later be shown in Section 3.3 to be consistent with the 3D CFD results.

2.1.2. Axisymmetric throughflow The design of the centerbody is also critical to effective open rotor design. In particular, the regions nearest the hub have a strong tendency to have high compressibility losses because of the low blade-to-blade spacing as well as the large thickness necessary at the hub for structural reasons. These can be mitigated somewhat by appropriate design of the hub by incorporating area-ruled contouring intended to decrease the local Mach number near the points of highest blockage within the blade rows.

Such effects can be analyzed for preliminary design with an axisymmetric throughflow method. For this work, Multi-passage ThroughFLOW (MTFLOW) [36] was utilized. This code solves for the inviscid streamsurfaces surrounding an axisymmetric body, coupled with a viscous boundary layer computation on the surface. The rotor and stator are represented as distributed stage blocks, which apply swirl, work, losses, and blockage over an area representative of each blade row. Computational grids were created using 70 streamlines and 500 streamwise grid points, and convergence was detected when all flowfield residuals were smaller than 5.0×10^{-6}.

The initial hub surface was simply an elliptical nose mated

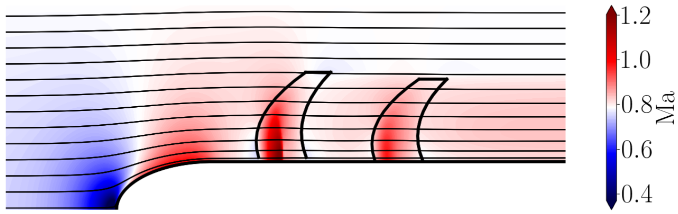

(a)

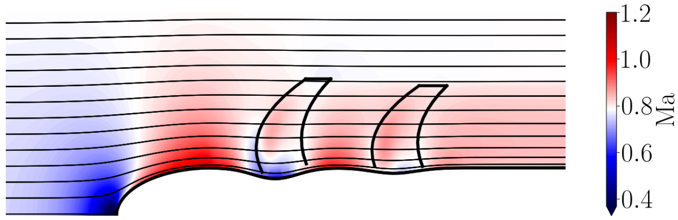

(b)

FIGURE 6: Mach number and every 5th streamline predicted by MTFLOW axisymmetric throughflow solver. Colormap center is set to Ma$_\infty$ = 0.785. a) no hub contouring, b) with hub contouring.

to a cylindrical sting. Hub contouring, in the form of multiple Gaussian "bumps" (actually divots because they decreased the hub radius), was then applied. The hub profile can be described by:

$$r(z) = r_{\text{baseline}}(z) + r_{\text{bumps}}(z) \tag{1a}$$

$$r_{\text{baseline}}(z) = \begin{cases} r_{\text{hub}}\sqrt{1-[z/(2r_{\text{hub}})]^2} & z < 0 \\ r_{\text{hub}} & z \geq 0 \end{cases} \tag{1b}$$

$$r_{\text{bumps}}(z) = A_1 e^{-(z-b_1)^2/w_1^2} + A_2 e^{-(z-b_2)^2/w_2^2} \tag{1c}$$

where r_{hub} is the nominal hub radius (35% of the tip radius, or 0.934 m).

The parameters A_i, w_i, and b_i describe the depth, width, and location of the bumps. The values of these parameters were explored in order to decrease the maximum Mach number within each blade row (initially occuring at the points of maximum blade thickness), while still maintaining reasonable boundary layer characteristics. The blade row parameters (chord length, thickness, etc.) were held constant throughout this analysis. The selected maximum bump depth for the rotor blade row was 8% of the tip radius, while the maximum depth for the stator was 4% of the tip radius.

Figure 6 shows the axisymmetric spinner geometry, stage blocks representing each blade row, and predicted Mach number distributions throughout the flow for this contour profile compared to the equivalent case with no hub contouring. The contouring successfully kept the Mach number subsonic within both blade rows, even in the areas of highest blockage at the hub. It is worth noting that this does not mean that the actual 3D flow will not have local supersonic regions (as will be seen from the blade-to-blade and 3D CFD), but it does correspond to a substantial reduction in shock losses relative to the spinner without contouring. These contour parameters were held fixed for the remainder of this work.

2.1.3. Quasi-3D blade-to-blade CFD High performing blade section geometry is also needed to create an efficient open rotor stage. It is possible to create a design using a standard airfoil family: for example, the ONERA-SE design presented by Dumont [37] used airfoils from the NASA-SC2 supercritical airfoil family [38]. However, additional performance can be achieved by designing new airfoil profiles specifically tailored for the local blade conditions. Much prior work has considered methods of optimizing airfoil sections for a given purpose by taking advantage of computational analysis of cascade performance. One early example of this is the development of Controlled Diffusion Airfoils by Hobbs and Weingold [39]. A more recent example by Hergt et al., taking advantage of the improvements in computational resources of the last 40 years, lead to the creation of the Load Splitting Airfoil concept for highly loaded compressors [40]. Even though 3D optimization of airfoil blades is now viable, and has been for over 20 years [41], 2D analysis and optimization is still valuable. Due to the lower computational requirements, 2D results may be obtained more rapidly and more design parameters may be explored. Additionally, for flow features that are well-captured by 2D flow, the 2D results can sometimes serve to give physical insights that are more difficult to understand from the full 3D flow.

For this study, the 2D blade-to-blade solver MISES [42, 43] was used for airfoil optimization. MISES solves for the flow for blade sections that have been mapped to an $m' - \theta$ streamsurface coordinate system, and can additionally account for the effects of streamsurface thickness and radius changes. In the present work, the axisymmetric stream surfaces from MTFLOW were input into MISES, enabling the effect of the hub contouring to influence the blade-to-blade results. A coupled inviscid streamline and boundary layer method is used, and e^n and Abu-Ghannam-Shaw models are used to predict transition locations. The inlet turbulence intensity (required for transition modeling) was chosen to be 1% for the rotor during cruise. Due to disturbances from the rotor, the inlet turbulence for the stator was estimated as 3% at cruise.

Grids for MISES were generated using 20 streamlines each, and 90 streamwise grid points on the airfoil surfaces. Typically this produced about 200 total streamwise grid points at midspan. This grid size allowed rapid evaluation while keeping the loss coefficient within 3% of the values obtained by much finer grids (40 streamlines by about 400 streamwise grid points). Convergence was detected when the density and node positions change by no more than 5.0×10^{-5} RMS, and the viscous variables change by no more than 5.0×10^{-4} RMS (the default MISES convergence criteria). If convergence was not obtained within 65 iterations, the case was considered to have failed. Where possible, failed cases (due to lack of convergence or due to grid generation failures) were filled in via linear interpolation from their neighbors. Most grid generation failures were seen between 80% span and 90% span, where the leading edge of one blade is closely aligned with the trailing edge of its neighbor, which can confuse the grid generator. If more than 10% of MISES cases failed for a particular blade, that geometry was considered to have failed and was not considered as a viable candidate design. The only MISES failures on the final rotor occured at section #36 (87% span) and

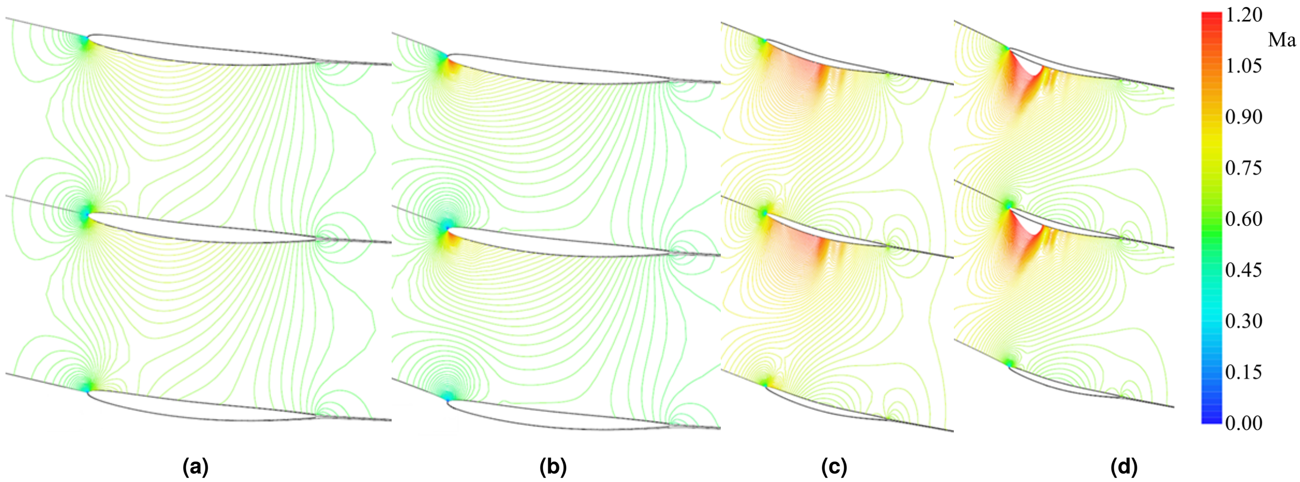

FIGURE 7: Mach number distributions from MISES blade-to-blade solver. a) hub, on-design incidence, b) hub, off-design incidence (+7.0°), c) mid-span, on-design incidence, d) mid-span, off-design incidence (+4.6°).

were filled in by interpolating the values at sections #35 and #37.

In order to ensure sufficiently robust performance, MISES was run both at design conditions and at an off-design incidence. Off-design performance may be especially critical for open rotors due to climb requirements: not only will the incidence change due to the changes in rotor speed and re-stagger, but the nonzero angle-of-attack during climb will cause significant incidence swings during each blade rotation. An example output from MISES, showing Mach number contours for two different sections of the N-OPEN-1 rotor, is shown in Fig. 7. The objective function for optimization (which will be introduced in Section 2.4) includes the loss at the design incidence and at the off-design incidence.

2.2. Structural analysis

In order to incorporate structural considerations into the preliminary design process, Finite Element Analysis (FEA) was performed using Ansys Mechanical [44]. For preliminary design and optimization, linear static structural analyses that only considered centrifugal loading were conducted. After optimization, a modal analysis was performed in order to determine a preliminary Campbell diagram.

2.2.1. Static structures The workflow was automated using Python scripting in Ansys Workbench in order to facilitate use in the optimization routine. To simplify the geometry, the blade was attached to a large wedge, which was constrained at its base. A 0.5 inch (12.7 mm) fillet was applied at the blade-wedge interface using Ansys DesignModeler. The mesh was intentionally coarse to facilitate rapid simulation turnaround: a typical model for design optimization consisted of approximately 85,000 nodes and 50,000 elements. Local sizing on the blade face and fillet was defined in terms of the global element size parameter. The mesh sizing was set to 20% of the global element size on the blade face and 10% on the fillet. The global element size was automatically adjusted by Ansys Mechanical, ensuring that the template accommodates geometries of any scale. Additionally, the curvature normal angle was set to 45°, the curvature minimum size was 5% of the global element size and the growth rate was 1.3.

The material chosen for this design was 7075-T6 aluminum alloy, which was chosen to reduce the complexities that a composite design would have. Material properties were obtained from MatWeb [45] and are shown in Table 3.

	Al 7075-T6	
Density ρ	2810	$\mathrm{kg/m^3}$
Elastic modulus E	71.7	GPa
Poisson's ratio ν	0.33	
Tensile yield strength σ_y	503	MPa

TABLE 3: Material properties used in Ansys Mechanical.

The model was constrained on the sides and bottom of the wedge, as shown in Fig. 8. Centrifugal loading was applied at $97.0\,\mathrm{rad\,s^{-1}}$ (926 RPM); this represents the rotational speed at takeoff, which is anticipated to be the most extreme loading condition. For this reason, Table 3 is for standard day conditions rather than at cruise altitude. The results are described in terms of the Factor of Safety (FS), which was calculated using the maximum von-Mises stress in the model $\sigma_{vm,max}$ and the yield strength of the material σ_y:

$$\mathrm{FS} = \frac{\sigma_y}{\sigma_{vm,max}} \tag{2}$$

A mesh refinement study is needed to assess the level of mesh independence of the solution, and was conducted by reducing the element size, growth rate, and curvature normal angle parameters within Ansys Mechanical. Table 4 details the results of the mesh refinement study. FS is shown to decrease with each level of mesh refinement, indicating that the coarse mesh used for design underpredicted the maximum stress by approximately 11%. The maximum stress occurred in the fillet for each model. While the high stress in the fillet could easily be mitigated by increasing the fillet radius, the final design will not utilize a bladed disk, as the blade requires pitch actuation. Consequently, the final design will incorporate a trunnion and attachment hardware. Work is currently underway to improve the structural analysis to better represent the hardware required for the final design. Contours

Mesh	Element Size	Growth Rate	Curvature Normal Angle	Nodes	Elements	Factor of Safety
Baseline	0.1520	1.300	45.0°	84 449	50 649	1.78
Refinement 1	0.0750	1.150	22.5°	519 300	343 081	1.65
Refinement 2	0.0375	1.075	11.2°	3 580 212	2 502 068	1.60

TABLE 4: Static structural mesh refinement study.

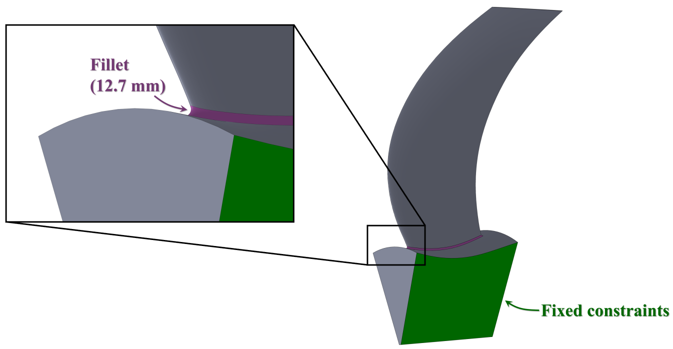

FIGURE 8: N-OPEN-1 rotor blade showing the fillet and highlighting the surfaces used to fix the model.

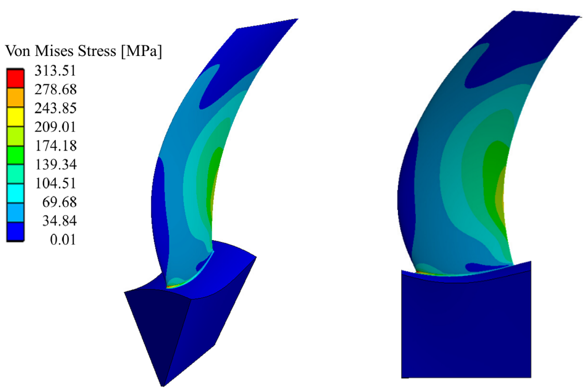

FIGURE 9: Contours of von Mises stress on N-OPEN-1 rotor blade.

of von Mises stress calculated using the most refined mesh are illustrated in Fig. 9.

2.2.2. Dynamic structures Structural dynamics analysis is also a critical component of the open rotor design process, essential for avoiding destructive resonance. The fundamental tool used to assess the vibrational characteristics of a rotor is the Campbell diagram [46], which plots vibrational modes of the rotor against multiples of the rotational speed (engine orders, EO). To construct a Campbell diagram, a modal analysis of the N-OPEN-1 geometry was conducted in Ansys Mechanical using the baseline mesh described in Section 2.2.1. The analysis swept the rotational velocity in 100 RPM increments up to the takeoff speed, extracting the first four modes. It is important to note that this model did not utilize cyclic symmetry boundary conditions; therefore, nodal diameter (ND) patterns were not explicitly considered. However, the results closely approximate those expected for a 4ND pattern.

Figure 10 is the Campbell diagram that presents the results

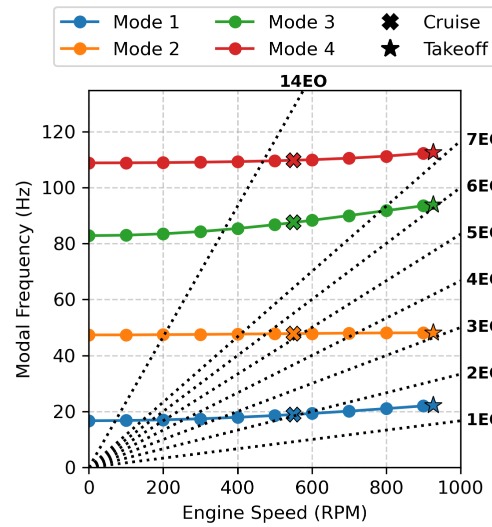

FIGURE 10: Campbell diagram for N-OPEN-1 rotor.

of this process. The data highlights several potential resonance concerns that must be addressed before the design is finalized. Of primary concern are the 2EO line, which crosses Mode 1 at cruise engine speed, and the 3EO line, which crosses Mode 2 at takeoff speed. Additionally, the 7EO line approaches the value of Mode 4 at takeoff. This is particularly critical given that the seven stators located downstream of the rotor could induce 7EO excitation. These findings highlight the importance of a design iteration to mitigate the risk of high-cycle fatigue failure. This will be addressed as the design is updated to incorporate the blade geometry required for the trunnion system that is planned for the final design. Other future work will be needed to assess aeromechanical concerns such as flutter.

2.3. Acoustics

While no optimization was performed in order to directly improve acoustics as part of this work, several important considerations for acoustics were included.

The stator was chosen to be 95% the tip radius of the rotor so that the shed tip vortices from the rotor would pass around the stator, reducing interaction tones. These tones are affected by the blade counts, and using 9 rotor blades and 7 stator vanes avoids any common factors that may exacerbate interaction tones. Additionally, the optimization of the rotor airfoils to reduce losses will weaken the rotor wakes, also reducing interaction tones. The fairly long spacing (approximately 0.6 r_{tip}) between the rotor and stator should also help these wakes partially mix out prior to impinging on the stator. This long rotor–stator spacing is more achievable without major weight penalties on an open rotor stage than on a counter-rotating open rotor, because power does not need to be transmitted to both blade rows. Future work will consider optimization of this spacing, including tradeoffs between acoustic and aerodynamic performance.

Significant tip sweep was also applied, using the lessons learned from the SR-3 and similar rotors (which has a dual aerodynamic and aeroacoustic benefit). One of the many benefits of sweep is that it can cause parts of the loading noise to be out-of-phase, resulting in destructive interference [6].

Lastly, the selection of a high advance ratio (low rotor speed) is perhaps the most important design consideration for acoustics in this paper. This is only possible due to the presence of the stator to remove exit swirl; without it, the propulsor would lose an unacceptably high portion of the input power to residual swirl (greater than 15% in the current study). By recovering most of this energy through the stator, the rotor can be run at a lower speed. The blade tips can remain subsonic throughout the flight envelope.

2.4. 2D section optimization

Many of the blade parameters used for aerodynamic optimization of blade sections also have significant impact on structural performance. This is especially true for the blade thickness and chord length. As a result, it is important to ensure that adequate structural strength is retained even as the section properties change. To handle this challenge, an objective function that combined aerodynamic and structural performance was used:

$$f(\boldsymbol{x}) = f_{\text{aero}}(\boldsymbol{x}) + f_{\text{structural}}(\boldsymbol{x}) \tag{3}$$

where $\boldsymbol{x}$ is the 45-element vector of design variables active during the 2D optimization of each blade row.

The structural portion of the objective function is designed to contribute strongly when the factor of safety is below an acceptable value (1.70 for this work), but to drop out entirely when acceptable. By implementing this "soft constraint" on factor of safety, optimizers with no explicit representation for constraints could still be explored with the same objective function.

$$f_{\text{structural}}(\boldsymbol{x}) = \begin{cases} 1000(\text{FS} - 1.70)^2 & \text{FS} < 1.70 \\ 0 & \text{FS} \geq 1.70 \end{cases} \tag{4}$$

For speed, the coarsest mesh considered in Section 2.2 was used to evaluate the factor of safety throughout optimization. Additionally, due to uncertainties at the time on the aluminum alloy to be used, the optimization was carried out with slightly different material properties (E = 73.1 GPa, ρ = 2840 kg/m^3, and σ_y = 498 MPa) than the final analysis. The optimized design was then checked with the mesh refinement study and material properties discussed in Section 2.2 (E = 71.7 GPa, ρ = 2810 kg/m^3, and σ_y = 503 MPa).

Aerodynamic performance is quantified by the loss coefficients at on-design and off-design incidences, as well as the exit deviation at on-design incidence. The loss coefficient reported by MISES for this work is a total pressure loss coefficient, equal to the total pressure losses across the row normalized by the dynamic pressure upstream of the row [43]:

$$\overline{\omega} = \frac{Pt_2^{\text{isen}} - \overline{Pt_2}}{Pt_1 - P_1} \tag{5}$$

where $\overline{Pt_2}$ represents the mixed-out total pressure downstream of the blade row.

For the present work, the loss term of the objective function is simply the sum of the loss coefficients across all blade sections. The deviation term was equal to the sum of squares of all errors in the exit flow angle relative to the target (in degrees). The weights of each term were selected such that the influence of each term was approximately equal when the deviation was around 1 degree. This led to a behavior where the optimizer would quickly drive the deviation below one degree (even at the cost of a slight increase in loss), before slowly reducing the losses as the solution converged.

$$f_{\text{aero}}(\boldsymbol{x}) = 100 f_{\text{loss}}(\boldsymbol{x}) + f_{\text{deviation}}(\boldsymbol{x}) \tag{6a}$$

$$f_{\text{loss}}(\boldsymbol{x}) = \sum_{i}^{n_{\text{sections}}} \left[\overline{\omega}_i(\text{design}) + \overline{\omega}_i(\text{off-design})\right] \tag{6b}$$

$$f_{\text{deviation}}(\boldsymbol{x}) = \sum_{i}^{n_{\text{sections}}} \left[\beta_{2,i}(\text{design}) - \beta_{2,i}(\text{target})\right]^2 \tag{6c}$$

Some additional performance could likely be gained by using a more physically meaningful objective function. For example, the distribution of loss coefficients along the blade span could be used to determine an overall entropy rise across the row, and the exit deviation errors could be used to calculate the power lost to undesired swirl. These could then be combined into an overall efficiency estimate for use in the objective function.

As each section is independent for the blade-to-blade analysis, MISES can be run simultaneously in parallel on as many sections as computational resources allow. MISES solutions are also independent of FEA solutions. This allows rapid solutions for the performance of the entire blade (41 sections for the rotor in the current analysis). Various optimization techniques were explored, the most effective of which have been Sequential Least Squares Programming (SLSQP) [47], implemented within SciPy, and a Bayesian optimization technique, implemented within Ax [48]. The present design, N-OPEN-1, was optimized with SLSQP. As a gradient-based technique, SLSQP requires accurate derivative information. This was obtained by using relatively large step sizes for finite differences, in order to overcome numerical errors in both the aerodynamic and structural calculations. A total of 886 rotor designs were analyzed over a period of about 48 hours of wall-clock time. For comparison, the Bayesian optimization method required about 1000 Sobol' sequence samples to initially sample the design space, followed by thousands of Bayesian trial points to obtain comparable results to SLSQP. This is why SLSQP was selected for this design, though Bayesian (and other) optimization methods may prove advantageous on other related problems. Over the course of the SLSQP optimization, the factor of safety was increased from 1.323 to 1.703 (just above the soft constraint), the root-mean-square deviation fell from 1.23° to 0.43°, and the average loss coefficient decreased by 9.4%.

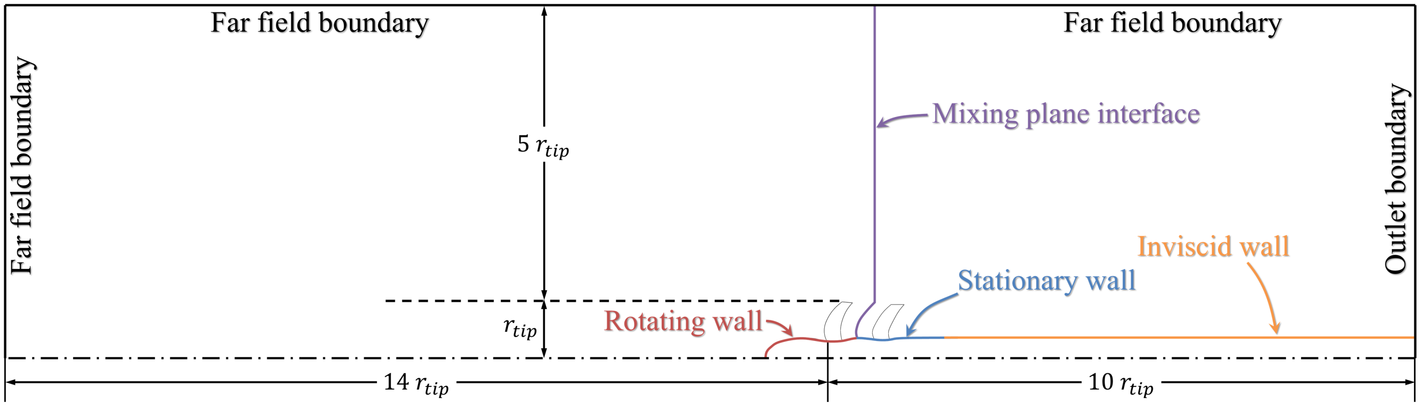

FIGURE 11: Computational domain with far-field boundary positions and hub details.

Structural performance was not considered for the stator ($f_{\text{structural}}$ was set to 0), as there are no rotational loads to consider. With no structural constraint, the stator thickness was driven by the need for sufficient incidence tolerance (and it was not driven to the minimum allowable by the constrained optimization). Other than this change, stator optimization proceeded identically to rotor optimization, except significantly faster due to not requiring FEA solutions and due to the lower relative Mach numbers (which enabled faster convergence of MISES). Without having to compromise for structural performance, aerodynamic optimization was also more effective. RMS deviation was driven from 0.95° to 0.06°, and the average loss coefficient was decreased by 37%.

A related process was previously used to design a supercritical CO_2 compressor stage [49] that was later evaluated experimentally [50]. The core difference between the process used in that prior work and the current effort is that the prior work did not simultaneously consider aerodynamics and structures. Performing section optimization without considering structures is simpler, and allows each section to be optimized sequentially instead of simultaneously. However, it does not allow proper tradeoffs to be made (for example, aerodynamics will generally drive towards thinner blades while structures will drive towards thicker blades). The present work simultaneously evaluates aerodynamic performance at all blade sections and structural performance of the entire blade, allowing effective tradeoffs.

3. 3D CFD

Once a candidate design has been created, it must be evaluated with 3D CFD to verify performance. While 2D tools are powerful, there are some effects that are only properly captured in 3D. The performance of the optimized design at the cruise condition (the primary design point) was evaluated using 3D steady RANS CFD. Climb performance was not assessed with CFD as part of this work. Accurate computation of the climb case will require either full-annulus unsteady or nonlinear harmonic CFD, in order to capture the effects of incidence swings between the advancing and retreating blades. While takeoff could be analyzed in mostly the same way as cruise, takeoff results will instead be presented alongside climb-out results.

3.1. Mesh

Computational grids were generated using Cadence AutoGrid5. A multi-block O4H structured topology was applied to the single-passage unducted rotor and stator domains, connected by a mixing plane interface. The O4H topology places an O-grid around the blade profile and is enclosed by four H-grid blocks positioned upstream, downstream, above, and below the blade. This configuration is well suited for turbomachinery applications due to its ability to resolve boundary layers near blade surfaces while maintaining mesh quality elsewhere in the flowfield domain. A multi-grid strategy is used, which facilitates efficient analysis and mesh studies. The use of template mesh configurations maintains topological consistency across all design cases, ensuring accurate comparative analysis between geometries.

At the finest grid level, the mesh is composed of approximately 66 million points. Wall cell heights on the blade surfaces were calculated to achieve a y^+ value below 1. Illustrated in Fig. 11, the inlet, outlet, and far field are positioned, respectively; 14, 10, and 5 rotor tip radii from the rotor blade.

A total of 4 grid levels were generated, with an average refinement ratio of approximately 2. A grid convergence study was performed using the finest 3 grid levels. The Grid Convergence Index (GCI) suggested by Roache [51] was used to quantify the numerical uncertainty due to discretization errors in the CFD solution. With Roache's "factor of safety" parameter set to 1.25, GCI was calculated to be 1.46% for total thrust and 0.63% for rotor torque.

3.2. Domain and solver

The 3D RANS flow solver used for CFD simulations was Cadence FINE/Turbo [52]. The Spalart-Allmaras turbulence model is intended to be used for future optimizations, and was used for the grid convergence study. However, additional analyses were run with the $k-\omega$ SST model on the finest grid to examine the solution with improved near wall accuracy. Fully turbulent and transitional (using the Menter and Langtry $\gamma-\mathrm{Re}_{\theta t}$ transition model [53]) $k-\omega$ SST solutions were generated. Solution numerical convergence was monitored using two criteria: a decrease in the global Navier-Stokes residuals of greater than 6 orders of magnitude from the initial state, and the stabilization of blade force, hub force, and rotor torque, which reached minimal

Grid points	Turbulence model	Net efficiency	Total thrust	Rotor thrust	Stator thrust	Rotor torque
155,778	Spalart-Allmaras	78.89%	20.85 kN	18.25 kN	2.607 kN	106.6 kN m
1,120,861	Spalart-Allmaras	80.93%	21.08 kN	18.31 kN	2.770 kN	105.1 kN m
8,740,726	Spalart-Allmaras	83.07%	22.00 kN	18.86 kN	3.137 kN	106.9 kN m
67,317,610	Spalart-Allmaras	82.27%	21.63 kN	18.62 kN	3.011 kN	106.1 kN m
67,317,610	k-ω SST	83.03%	22.02 kN	18.84 kN	3.182 kN	107.0 kN m
67,317,610	k-ω SST + transition	84.70%	22.95 kN	19.57 kN	3.386 kN	109.3 kN m

TABLE 5: Efficiency and thrust for N-OPEN-1 at cruise reported by 3D CFD.

fluctuations over iterations.

The external flow boundary condition was used at the inlet and far field, allowing for the specification of free stream velocity components, along with static pressure and temperature. The turbulence intensity of 1.0% matched the MISES blade-to-blade CFD input and is the value suggested by Cadence for external flow simulations. The outlet boundary condition was imposed as static pressure.

Shown in Fig. 11, the blades and the portion of the hub near the blades were modeled as adiabatic, no-slip walls. An inviscid wall was applied to the aft portion of the hub, extending from 1.5 stator tip radii downstream of the stator trailing-edge to the outlet. This was done to prevent artificial boundary layer growth at the hub towards the outlet. A mixing plane was used at the rotor-stator interface, which extended into the far field.

3.3. Results

Design cruise conditions from Table 1 were used: a free stream Mach number of 0.785 and atmospheric properties corresponding to an altitude of 10,668 m (35,000 ft). The rotor rotation speed was set to 57.7 rad/s (551 RPM).

The primary metric for the efficiency of the open rotor stage in this work was the net efficiency discussed in [7] (also called the aero-propulsive efficiency in [37]), defined as the ratio of the propulsive power to the shaft power:

$$\eta_{NET} = \frac{\text{thrust} \cdot V_\infty}{\text{torque} \cdot \Omega} \tag{7}$$

Note that when considering propulsion-airframe integration it may be necessary to use some other metric for the propulsive power, as thrust is not necessarily well-defined for the integrated system. However, for the purposes of this paper, we will only consider the propulsor in isolation. Even in this case, appropriately defining the thrust is not entirely obvious. For example, the computational work on the ONERA-SE [37] simply took the forces on the blade surfaces, ignoring the forces on the nacelle. In contrast, the experimental SR-3 work [7] took the thrust to be the difference between the force exerted by the nacelle+rotor system and the drag force exerted by the nacelle without the rotor installed. In general (but perhaps not universally), the approach taken by ONERA will lead to a higher estimate of thrust (and efficiency) due to the mutual interaction between the rotor and the nacelle, which contributes to the force on the rotor blades but does not contribute to propelling the aircraft (as it is equal and opposite between the two components). For consistency with the ONERA-SE analysis, we will consider thrust to be equal to the sum of axial forces on all blades, and torque will be integrated over the rotor surfaces only (neglecting any viscous torque on the rotating portion of the hub).

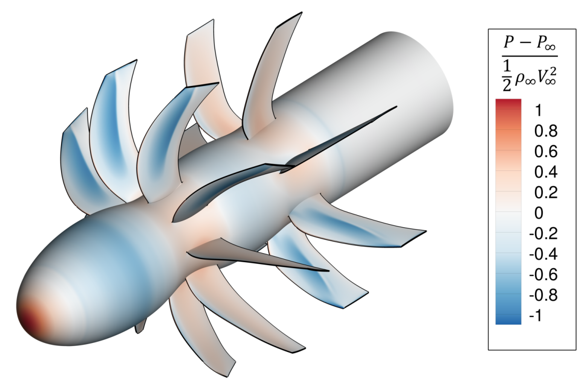

FIGURE 12: Static pressure coefficient contours on N-OPEN-1.

Static pressure coefficient contours for the $k-\omega$ SST + transition solution are presented in Fig 12. The suction side contours on both sets of blades show the flow accelerating over the leading edge to the front-to-mid chord. The pressure significantly drops in this region, which corresponds to the peak velocity. The shock surface is visible as a sudden rise in pressure coefficient. From mid-chord to the trailing edge, flow diffuses without separation (no regions of negative velocity were observed near any blade surfaces). The effect of the hub contouring is also clearly visible, with static pressure increases in both blade rows corresponding to the areas of decelerated flow caused by the contouring.

Table 5 summarizes results across all grid levels and turbulence models. The $k-\omega$ SST model predicts a net efficiency of 84.70% when transition is included, compared to 83.03% for the fully-turbulent solution. This significant gain highlights the impact of resolving laminar flow regions on the blade surfaces, which reduces skin friction drag. For the fully-turbulent models, the $k-\omega$ SST model predicts slightly higher loading and efficiency than the Spalart-Allmaras model on the finest grid. Regardless of turbulence model, the predicted net efficiency is significantly higher than that of the recently published ONERA-SE design (78.0%) [37], despite the higher cruise Mach number (0.785 for N-OPEN-1 vs. 0.750 for ONERA-SE).

Thrust is predicted to be 22.95 kN with transition (22.02 kN without) significantly above the 18.3 kN requirement. Reducing the loading to match only the required thrust would likely come with a benefit to efficiency. Alternatively, loading could be maintained and the rotor size reduced. The rotor contributes 85.2% of this total, and the stator 14.8%. This can be compared against

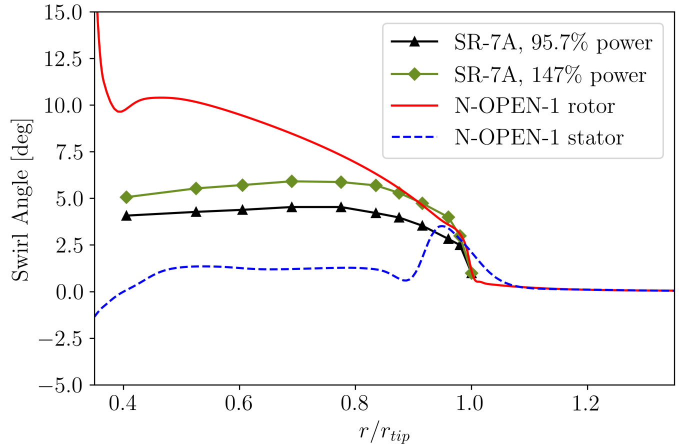

FIGURE 13: Mass-averaged swirl angles for N-OPEN-1, compared against experimental data on SR-7A rotor by Stefko et al. [10].

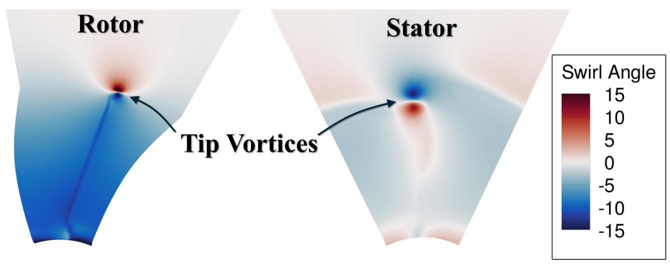

FIGURE 14: Swirl angle distributions for N-OPEN-1 downstream of rotor (just upstream of mixing plane) and downstream of stator.

the 9% thrust fraction made by the stator of the ONERA-SE, and with the optimized designs analyzed by Sala et al. (approximately 10% thrust generated by the stator) [54].

This thrust split is enabled by the relatively high swirl leaving the rotor, as shown in Fig. 13, which plots mass-averaged swirl angle as a function of radius. Excluding the boundary layer, the maximum swirl of 10.4° occurs at about 0.46 r_{tip} (about 17% span). Contrast this with the swirl produced by the SR-7A rotor, which was less than 6 degrees even at 147% of design power [10]. This low level of exit swirl was beneficial when operating SR-7A as an isolated propeller (as it was designed to be). However, it also means there is very little swirl kinetic energy in the exhaust stream for the stator to recover. This is a primary reason for the low effectiveness of the swirl recovery vanes tested with SR-7A by Gazzaniga et al. [13], which produced less than 4% the thrust of the rotor at the design point and produced more drag than thrust at only slightly off-design conditions. N-OPEN-1 is designed to produce nearly a free vortex swirl (i.e., inversely proportional to radius), modified to include some falloff in swirl at the tip and hub. The near free vortex keeps the work distribution more uniform than it would be for a typical single-rotation propeller like SR-7A, which is highly tip-loaded. The N-OPEN-1 rotor would be worse than SR-7A if it were used in isolation: considering that swirl kinetic energy is proportional to the square of tangential velocity, this higher exit swirl represents a much greater fraction of the rotor power that would be wasted.

However, because N-OPEN-1 was designed from the beginning to be used with an exit stator, this exit swirl does not go to waste. The stator successfully holds the exit swirl below 1.5° at every radius below 0.90 r_{tip}. At the stator tip radius of 0.95 r_{tip}, where stator lift must go to zero, the swirl peaks at 3.5°, close to the value leaving the rotor. Close to the hub there is some overturning (caused by interaction with the boundary layer, which is now much thicker), and the stator actually produces some slightly negative swirl. Overall, the stator does a good job of straightening the flow, leaving very little swirl on average.

Figure 14 shows the swirl angles for a single periodic passage (1 of 9 for the rotor and 1 of 7 for the stator). In addition to the average swirl (substantially lower for the stator), the tip vortices are prominently visible. These also present a kinetic energy loss that decreases the amount of power that goes towards propelling the aircraft. Other nonuniformities, such as secondary flows near the hub and overturning in the rotor wake are also visible. Further insight into the performance of the rotor and stator, including the effects of these nonuniformities, can be obtained by using the power balance approach proposed by Drela [55]. This method was previously applied to open rotor propulsors by Schnell and Mennicken [56], who used it to make comparisons between ducted and unducted propulsors. Siddappaji [57] also applied the method to various unducted rotors (both propellers and wind turbines). We will follow the work done by these prior authors, but make adaptations where needed to give clearer insight into the open rotor stage design. The power balance method provides expressions for the mechanical power deposited in the exhaust stream. These are broken down into terms for streamwise kinetic energy, transverse kinetic energy, and pressure-defect work, all evaluated over a Trefftz plane downstream of the control volume:

$$\dot{E}_a = \iint \frac{1}{2}\rho w^2 \left(V_\infty + w\right) dS \tag{8a}$$

$$\dot{E}_v = \iint \frac{1}{2}\rho \left(u^2 + v^2\right)\left(V_\infty + w\right) dS \tag{8b}$$

$$\dot{E}_p = \iint \left(P - P_\infty\right) w dS \tag{8c}$$

Where the perturbation velocity $w = V_z - V_\infty$ represents the change in axial velocity relative to freestream, and u and v are the two transverse components (note that we have changed the symbols from the original work for consistency with the rest of this paper). We can rewrite the equation for the traverse losses in terms of polar coordinates as:

$$\dot{E}_v = \iint \frac{1}{2}\rho \left(V_\theta^2 + V_r^2\right)\left(V_\infty + w\right) dS \tag{9}$$

We may further break the transverse losses into an axisymmetric term (equal to what the transverse kinetic energy would be if the only transverse flow were the average swirl) and a non-axisymmetric term (containing primarily the tip vortices and other non-uniformities):

$$\dot{E}_v = \dot{E}_{v,\text{ax}} + \dot{E}_{v,\text{non-ax}} \tag{10a}$$

$$\dot{E}_{v,\text{ax}} = \iint \frac{1}{2}\rho \overline{V_\theta}^2 \left(V_\infty + w\right) dS \tag{10b}$$

$$\dot{E}_{v,\text{non-ax}} = \dot{E}_v - \dot{E}_{v,\text{ax}} \tag{10c}$$

	Turbulence model	$\dot{E}_a$	$\dot{E}_v$	$\dot{E}_{v,\mathrm{ax}}$	$\dot{E}_{v,\text{non-ax}}$	$\dot{E}_p$	η_{prop}	η_{trans}	η_{NET}
Rotor only	Spalart-Allmaras	4.34%	19.31%	16.88%	2.43%	-3.35%	77.71%	91.07%	70.77%
Rotor only	k-ω SST	4.53%	19.51%	17.10%	2.41%	-3.71%	77.74%	91.32%	70.99%
Rotor only	k-ω SST + transition	4.49%	19.85%	17.38%	2.47%	-3.62%	77.69%	92.88%	72.16%
Rotor + stator	Spalart-Allmaras	2.83%	3.91%	0.83%	3.08%	-0.21%	92.64%	88.75%	82.27%
Rotor + stator	k-ω SST	2.67%	3.79%	0.79%	3.00%	-0.18%	92.97%	89.26%	83.03%
Rotor + stator	k-ω SST + transition	2.82%	3.91%	0.78%	3.13%	-0.19%	92.84%	91.18%	84.70%

TABLE 6: Power balance accounting for N-OPEN-1 at cruise (normalized by the shaft power, torque · Ω).

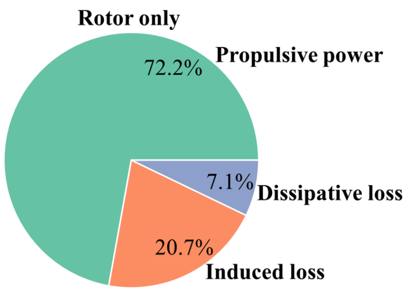

FIGURE 15: Loss breakdown for N-OPEN-1 before and after stator at cruise conditions ($k-\omega$ SST turbulence model with transition).

where the mass-weighted tangential velocity is:

$$\overline{V_\theta}(r) = \frac{\int_0^{2\pi} \rho \left(V_\infty + w\right) V_\theta d\theta}{\int_0^{2\pi} \rho \left(V_\infty + w\right) d\theta} \tag{11}$$

For this isolated propulsor, the axial forces are not balanced: a net thrust is produced to offset drag on the rest of the airframe. The full power balance, including this propulsive power, can be written as:

$$\text{torque} \cdot \Omega = \text{thrust} \cdot V_\infty + \dot{E}_a + \dot{E}_v + \dot{E}_p + \Phi \tag{12}$$

where Φ represents all dissipative effects (boundary layers, shocks, etc.). We may determine a propulsive efficiency as the ratio of propulsive power to the mechanical power including all induced losses as:

$$\eta_{\mathrm{prop}} = \frac{\text{thrust} \cdot V_\infty}{\text{thrust} \cdot V_\infty + \dot{E}_a + \dot{E}_v + \dot{E}_p} \tag{13}$$

Similarly, a transfer efficiency capturing the effect of dissipation can be determined as:

$$\eta_{\mathrm{trans}} = \frac{\text{torque} \cdot \Omega - \Phi}{\text{torque} \cdot \Omega} = \frac{\text{thrust} \cdot V_\infty + \dot{E}_a + \dot{E}_v + \dot{E}_p}{\text{torque} \cdot \Omega} \tag{14}$$

Defined in this way, the net efficiency in Eq. 7 is the product of the transfer and propulsive efficiencies:

$$\eta_{\mathrm{NET}} = \eta_{\mathrm{prop}} \cdot \eta_{\mathrm{trans}} \tag{15}$$

We evaluate all terms at a Trefftz plane 1.0 r_{tip} downstream of the stator in order to understand the performance of the complete stage. Additionally, we look at a plane immediately upstream of the mixing plane (about 0.3 r_{tip} downstream of the rotor trailing edge) in order to gain insight into the rotor-only performance. The complete results are shown in Table 6, and the breakdown for the $k-\omega$ SST case with the transition model is shown in Fig. 15. We see that the rotor would perform quite poorly in isolation, with a propulsive efficiency of only 77.7%, leading to a net efficiency of only about 72%. This is driven by the large swirl leaving the rotor, which carries away over 19% of the input power as swirl kinetic energy. Most of this (about 17%) is axisymmetric, and is successfully recovered by the stator, which leaves less than 1% of the input power as axisymmetric swirl. The stator does come with a small dissipative loss penalty (resulting in about a 2% reduction in transfer efficiency), but this is more than made up for by the reduced swirl losses. With the stator, the propulsive efficiency is almost 93%, enabling the high net efficiency of 84.7% for the $k-\omega$ SST case with transition. Tip vortex losses exiting the stator are approximately 3%.

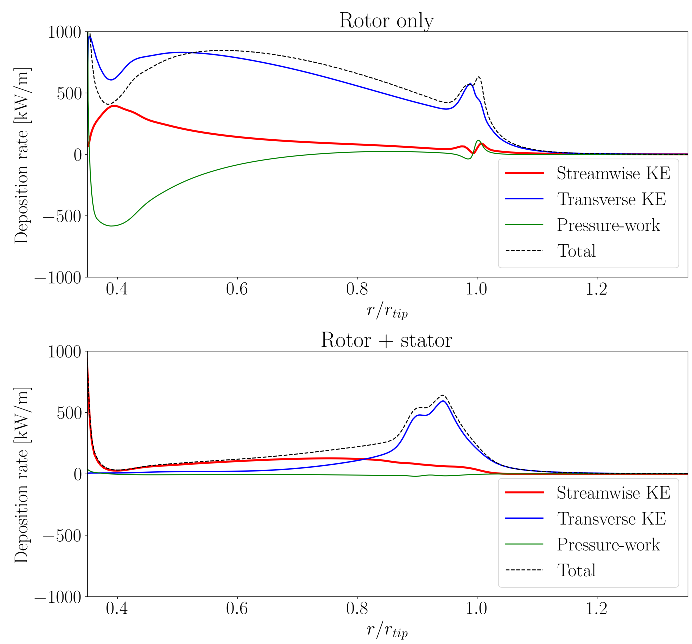

FIGURE 16: Decomposition of induced loss as a function of radius, before and after the stator at cruise ($k-\omega$ SST with transition).

Figure 16 shows the induced loss terms (the integrands of $\dot{E}_a$, $\dot{E}_v$, and $\dot{E}_p$) as a function of radius, weighted by circumference so that each curve represents the loss per unit radius. Once again, we see the strong loss contribution of the swirl downstream of the rotor, and see that it is mostly removed by the stator. The contribution of the tip vortices is also clear near 1.0 r_{tip}. This plot helps make sense of the negative contribution of the pressure-work term (-3.62% downstream of the rotor): the low pressure is associated with radial equilibrium required for the swirling flow. There is a locally high level of streamwise (i.e., axial) kinetic energy losses in this low static pressure region, partially offsetting it. Downstream of the stator, streamwise kinetic energy losses are low and relatively uniform. This is a primary motivation for using an open rotor: the large diameter allows a large volume of air to be accelerated only slightly, minimizing the wasted kinetic energy in the axial direction. Overall, the primary way to further improve the induced losses (and therefore the propulsive efficiency) would be to reduce the strength of the tip vortices. Note that the rotor tip vortices do not show up in the stator induced loss breakdown, as they have been mixed out by the mixing plane, but instead show up as dissipative losses. The 3.13% of shaft power associated with non-axisymmetric transverse flow only includes the stator tip vortices, and an estimate including the rotor would be higher.

Very little difference between the turbulence models is observed in the mechanical power terms or in the calculated propulsive efficiency. This is as expected, because the presence of laminar flow on part of the blades mostly results in reduced profile losses (and a correspondingly higher transfer efficiency). Predictions of propulsive efficiency can therefore be confidently done with either turbulence model. The simple Trefftz plane model from Section 2.1.1 was also mostly accurate, predicting that the rotor would waste 22.8% of its input power as swirl kinetic energy and that the stator would reduce this waste to 2.97% (compare to 19.85% and 3.91%, respectively, for the $k-\omega$ SST model with transition). These findings will simplify design revisions for the purpose of reducing induced losses.

Figure 17 examines the laminar flow by plotting the intermittency near the surface of the blades. The large laminar region on the suction side of the rotor (persisting until the shock) is the primary cause of these reduced profile losses. Some irregularity in the transition location is seen on the stator between 20% and 50% span, and further work is needed to understand this. Recomputing the 3D CFD results with the Abu-Ghannam-Shaw transition model (rather than $\gamma - \mathrm{Re}_{\theta t}$), to enable direct comparison against the MISES blade to blade results, would be useful. Further work is also needed to investigate the robustness of these laminar flow features, including whether they can be maintained under realistic conditions of surface roughness and/or fouling. Nevertheless, the meaningful increase in net efficiency (1.7%) suggests that the design of laminar flow airfoils is worthwhile for this type of open rotor stage.

Overall, the 3D CFD shows that the optimized open rotor stage performs effectively. The flow leaving the rotor contains a high level of swirl, allowing slower rotation for a given amount of rotor work. This high level of exit swirl would be severely detrimental to the performance of the rotor as an isolated propeller. However, as part of an open rotor stage, the new rotor performs substantially better than typical single-rotation propellers like SR-7A.

4. CONCLUSIONS AND FUTURE WORK

N-OPEN-1, an open rotor stage design for a cruise Mach number of 0.785 at 35,000 feet (10,668 m) has been simultaneously optimized for aerodynamic and structural performance, primarily using two-dimensional aerodynamic methods. These 2D methods enabled a large number of design variables to be considered, facilitating a more thorough exploration of the design space. The optimized design was then evaluated with 3D CFD. Using a $k-\omega$ SST turbulence model, including transition, the net efficiency was estimated to be 84.7%. This efficiency is close to the values of 85–86% reported for several counter-rotating open rotors, suggesting that is possible to achieve comparable performance with an open rotor stage to a counter-rotating open rotor. Notably, the rotor for this new design is significantly different than a conventional single-rotation propeller. The swirl leaving the rotor is higher and less tip-loaded than the optimal single-rotation distribution. This allows the stator to produce a higher portion of the thrust than would be possible otherwise.

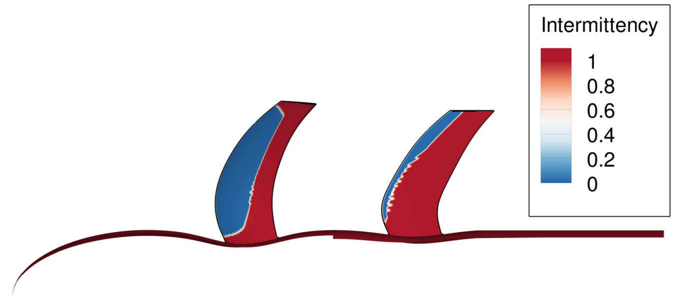

FIGURE 17: Intermittency on rotor suction side and stator pressure side predicted by Menter-Langtry $\gamma - \mathrm{Re}_{\theta t}$ transition model.

Future work is anticipated to raise the net efficiency further. In particular, optimization using 3D CFD to determine the best rotor and stator lean and to refine the blade tip shapes is expected to be useful. This is a key limitation of the current 2D-only optimization strategy: any truly three-dimensional effects cannot be properly designed for. However, the designs created with this strategy will serve as good starting points for further refinement by 3D optimization. A more highly optimized blade circulation distribution (taking into account the effect of losses) can bring further benefit. The current analysis showed that laminar flow may be able to significantly improve the net efficiency (1.7% in this work). Further investigation is needed to confirm this effect, and to enhance it if possible.

A full trade study of advance ratio and power loading, with optimized designs for each data point, would also be valuable. This trade study is enabled by the present work: the reliance on comparatively inexpensive two-dimensional computational tools to do the bulk of the optimization will allow the process to be repeated many times with different inputs. This trade study would help better understand realistic tradeoffs against rotor diameter, for example. Investigating the optimal design advance ratio may help mitigate tip losses. While the stator can recover the axisymmetric swirl, it cannot recover the tip vortices (which also increase in strength with the axisymmetric swirl). Running the rotor faster for a given power can weaken these tip vortices, though likely at the cost of viscous and shock losses on the blades. It is very possible that the true optimum for overall performance lies somewhere between this low-rotational speed design and a more conventional single-rotation propeller.

Additional structural analysis is also needed, including considerations for flutter. Future structural work will incorporate realistic trunnion geometry. Hot-to-cold transformation to determine required manufactured blade shapes, and cold-to-warm transformation to determine blade shapes at off-design conditions are also planned.

Detailed acoustic analysis and optimization is another future step. It is critical to properly characterize the self-noise and interaction noise of the rotor and stator, and to revise the design as needed to meet requirements. A key input to the acoustic analysis will be accurate CFD solutions for the climb-out condition at angle of attack. Climb-out will test the incidence tolerance of the rotor blades as they move from the advancing to the retreating side. This may require full annulus CFD solutions for confidence in the results, though nonlinear harmonic methods will also give some useful information. Further trade studies of aerodynamic vs. acoustic performance are anticipated.

ACKNOWLEDGMENTS

This work was funded by the NASA Advanced Air Transport Technologies project of the Advanced Air Vehicles Program, under the Aeronautics Research Mission Directorate.

REFERENCES

[1] Whitlow, J.B. and Sievers, G.K. "Fuel savings potential of the NASA Advanced Turboprop Program." *Aviation Fuel Conservation Symposium*: pp. 282–350. September 10-11, 1984. FAA, Washington, DC.

[2] Mikkelson, Daniel C., Mitchell, Glenn A. and Bober, Lawrence J. "Summary of recent NASA propeller research." *AGARD Fluid Dyn. Panel Meeting on Aerodyn. and Acoustics of Propellers*. NASA-TM-83733. October 1-4, 1984. Toronto, Canada.

[3] Hager, Roy D. and Vrabel, Deborah. "Advanced Turboprop Project." Special Publication NASA-SP-495. NASA. 1988.

[4] Van Zante, Dale E. "Progress in open rotor research: A US perspective." *Turbo Expo: Power for Land, Sea, and Air*. GT2015-42203. June 15-19, 2015. ASME.

[5] Metzger, F. and Rohrbach, C. "Aeroacoustic design of the Prop Fan." *5th Aeroacoustics Conference*. 79-0610. March 12-14, 1979. AIAA, New York, NY.

[6] Metzger, F.B. and Rohrbach, C. "Benefits of blade sweep for advanced turboprops." *Journal of Propulsion and Power* Vol. 2 No. 6 (1986): pp. 534–540.

[7] Rohrbach, C., Metzger, F.B., Black, D.M. and Ladden, R.M. "Evaluation of wind tunnel performance testings of an advanced 45 deg swept 8-bladed propeller at Mach numbers from 0.45 to 0.85." Contractor Report NASA-CR-3505. Hamilton Standard. 1982.

[8] Dittmar, James H., Stefko, George L. and Jeracki, Robert J. "Noise of the 10-bladed, 40 deg swept SR-6 propeller in a wind tunnel." Tech. Memo. NASA-TM-83054. National Aeronautics and Space Administration. 1982.

[9] Dittmar, James H., Stefko, George L. and Jeracki, Robert J. "Noise of the 10-bladed, 60 deg swept SR-5 propeller in a wind tunnel." Tech. Memo. NASA-TM-82950. NASA. 1983.

[10] Stefko, George, Podboy, Gary and Rose, Gayle. "Wind tunnel performance results of an aeroelastically scaled 2/9 model of the PTA flight test prop-fan." *23rd Joint Propulsion Conference*. AIAA-87-1893. June 29-July 2, 1987. San Diego, CA.

[11] DeGeorge, C.L., Turnberg, J.E. and Wainauski, H.S. "A report on the initial testing of the large scale advanced propfan." *22nd Joint Propulsion Conference*. AIAA-86-1551. June 16-18, 1986. Huntsville, AL.

[12] Campbell, William A, Wainauski, Harold S and Arseneaux, Peter J. "Large-scale Advanced Prop-fan (LAP) high speed wind tunnel test report." Contractor Report NASA-CR-182125. Hamilton Standard. 1988.

[13] Gazzaniga, John and Rose, Gayle. "Wind tunnel performance results of swirl recovery vanes as tested with an advanced high speed propeller." *28th Joint Propulsion Conference and Exhibit*. AIAA-92-3770. July 6-8, 1992. AIAA/SAE/ASME/ASEE, Nashville, TN.

[14] Wainauski, Harry S. and Vaczy, Carol M. "Aerodynamic performance of a counter rotating Prop-Fan." *22nd Joint Propulsion Conference*. AIAA-86-1550. June 16-18, 1986. Huntsville, AL.

[15] Chapman, D., Fleury, R. and Smith, D. "Testing of the 578-DX propfan propulsion system." *25th Joint Propulsion Conference*. AIAA-89-2581. July 10-12, 1989. Monterey, CA.

[16] Stuart, A. "The unducted fan engine." *21st Joint Propulsion Conference*. AIAA-85-1190. July 8-10, 1985. Monterey, CA.

[17] Hoff, GE. "Experimental performance and acoustic investigation of modern, counterrotating blade concepts." Contractor Report NASA-CR-185158. General Electric. 1990.

[18] Harris, Robert and Cuthbertson, R.D. "UDF™/727 flight test program." *23rd Joint Propulsion Conference*: pp. AIAA–87–1733. June 29-July 2, 1987. San Diego, CA.

[19] Van Zante, Dale E, Collier, Fayette, Orton, Arthur, Khalid, S Arif, Wojno, John P and Wood, Trevor H. "Progress in open rotor propulsors: The FAA/GE/NASA open rotor test campaign." *The Aeronautical Journal* Vol. 118 No. 1208 (2014): pp. 1181–1213.

[20] Schnell, R., Yin, J., Voss, C. and Nicke, E. "Assessment and Optimization of the Aerodynamic and Acoustic Characteristics of a Counter Rotating Open Rotor." *Journal of Turbomachinery* Vol. 134 No. 6 (2012).

[21] Zachariadis, Alexios, Hall, Cesare and Parry, Anthony B. "Contrarotating open rotor operation for improved aerodynamics and noise at takeoff." *Journal of Turbomachinery* Vol. 135 No. 3 (2013).

[22] Vlastuin, Jonathan, Dejeu, Clément, Louet, Anthony, Talbotec, Jérôme, Lepot, Ingrid, Lonfils, Timothée and Leborgne, Michaël. "Open rotor design strategy: from wind tunnel tests to full scale multi-disciplinary design." *Turbo Expo: Power for Land, Sea, and Air*. GT2015-43300. June 15-19, 2015. ASME, Montreal, Quebec, Canada.

[23] Smith, Dale A, Filippone, Antonio and Barakos, George N. "Noise source analysis in counter-rotating open rotors." *AIAA Journal* Vol. 60 No. 3 (2022): pp. 1783–1796.

[24] "Engine architecture - CFM International." Accessed 2025-11-16, URL https://www.cfmaeroengines.com/rise/engine-architecture.

[25] Betz, A. "The theory of the screw propeller." Technical Report No. NACA-TN-83. NACA. 1922.

[26] Goldstein, Sydney. "On the vortex theory of screw propellers." *Proceedings of the Royal Society A* Vol. 123 No. 792 (1929): pp. 440–465.

[27] Theodorsen, Theodore. "The Theory of Propellers I : Determination of the Circulation Function and the Mass Coefficient for Dual-Rotating Propellers." Tech. Report NASA-TR-775. NASA. 1944.

[28] Ribner, H. S. and Foster, S. P. "Ideal efficiency of propellers: Theodorsen revisited." *Journal of Aircraft* Vol. 27 No. 9 (1990): pp. 810–819.

[29] Smith, Jr., L. H. "Unducted fan aerodynamic design." *Journal of Turbomachinery* Vol. 109 No. 3 (1987): pp. 313–324.

[30] Siddappaji, Kiran, Turner, Mark G. and Merchant, Ali. "General Capability of Parametric 3D Blade Design Tool for Turbomachinery." *Turbo Expo: Power for Land, Sea, and Air*. GT2012-69756. June 11-15, 2012. ASME, Copenhagen, Denmark.

[31] Sharma, Mayank, Dannenhoffer, III, John F., Holder, Justin and Turner, Mark G. "Integration of an Open Source Blade Geometry Generator Using a Physics Based Parameterization With the Engineering Sketch Pad." *Turbo Expo: Power for Land, Sea, and Air*. GT2020-15943. September 21-25, 2020. ASME, Virtual, Online.

[32] Sharma, Mayank and Turner, Mark G. "Continuous Modified NACA Four-Digit Thickness Distribution for Turbomachinery Geometries." *AIAA Journal* Vol. 59 No. 4 (2021): pp. 1501–1505.

[33] Smith Jr, Leroy H and Yeh, Hsuan. "Sweep and dihedral effects in axial-flow turbomachinery." *J. Basic Eng.* Vol. 85 No. 3 (1963): pp. 401–414.

[34] Gümmer, V, Wenger, U and Kau, H-P. "Using sweep and dihedral to control three-dimensional flow in transonic stators of axial compressors." *Journal of Turbomachinery* Vol. 123 No. 1 (2001): pp. 40–48.

[35] Hanson, Donald B. "Compressible lifting surface theory for propeller performance calculation." *Journal of Aircraft* Vol. 22 No. 1 (1985): pp. 19–27.

[36] Drela, Mark. *A User's Guide to MTFLOW 2.01: Multi-passage ThroughFLOW Design/Analysis Program*. MIT Aerospace Computational Design Laboratory (2010).

[37] Dumont, Antoine. "Design of the open-rotor engine ONERA-SE for research application in aero-acoustic optimization." *ISABE 2024*. 2024-251. September 22-27, 2024. Toulouse, France.

[38] Harris, Charles D. "NASA supercritical airfoils: A matrix of family-related airfoils." Tech. Publication NASA-TP-2969. NASA. 1990.

[39] Hobbs, D. E. and Weingold, H. D. "Development of Controlled Diffusion Airfoils for Multistage Compressor Application." *Journal of Engineering for Gas Turbines and Power* Vol. 106 No. 2 (1984): pp. 271–278.

[40] Hergt, A., Reutter, O. and Grund, S. "A Novel Design Concept for Highly-Loaded Compressor Airfoils." *Journal of Turbomachinery* Vol. 147 No. 12 (2025).

[41] Benini, Ernesto. "Three-dimensional multi-objective design optimization of a transonic compressor rotor." *Journal of Propulsion and Power* Vol. 20 No. 3 (2004): pp. 559–565.

[42] Youngren, Harold and Drela, Mark. "Viscous/inviscid method for preliminary design of transonic cascades." *27th Joint Propulsion Conference*. AIAA-91-2364. June 24-26, 1991. AIAA/SAE/ASME/ASEE, Sacremento, CA.

[43] Drela, Mark and Youngren, Harold. *A User's Guide to MISES 2.63*. MIT Aerospace Computational Design Laboratory (2008).

[44] "Ansys Mechanical." ANSYS, Inc. Accessed 2025-11-18, URL https://www.ansys.com/products/structures/ansys-mechanical. Release 2025 R1.

[45] "Aluminum 7075-T6, 7075-T651." MatWeb. Accessed 2025-11-18, URL https://asm.matweb.com/search/specificmaterial.asp?bassnum=ma7075t6.

[46] Campbell, Wilfred. "The protection of steam-turbine disk wheels from axial vibration." *Transactions of the American Society of Mechanical Engineers* Vol. 46 (1924): pp. 31–140.

[47] Kraft, D. "A software package for sequential quadratic programming." Technical Report No. DFVLR-FB 88-28. DLR German Aerospace Center. 1988.

[48] Olson, Miles, Santorella, Elizabeth, Tiao, Louis C., Cakmak, Sait, Garrard, Mia, Daulton, Samuel and Lin, Zhiyuan Jerry et al. "Ax: A Platform for Adaptive Experimentation." *AutoML 2025 ABCD Track*. September 8-11, 2025. New York, NY.

[49] Ha, Matthew, Holder, Justin, Ghimire, Saugat, Ringheisen, Adam and Turner, Mark G. "Detailed Design and Optimization of the First Stage of an Axial Supercritical CO2 Compressor." *Turbo Expo: Power for Land, Sea, and Air*. GT2022-82590. June 13-17, 2022. Rotterdam, Netherlands.

[50] Ghimire, Saugat, Holder, Justin, Ha, Matthew, Turner, Mark, Kang, Jeongseek, Morris, Scott C, Sedlacko, Kyle and Held, Timothy J. "Numerical and Experimental Comparison of a Single Stage Axial sCO2 Compressor." *Turbo Expo: Power for Land, Sea, and Air*. GT2024-129128. June 24-28, 2024. ASME, London, United Kingdom.

[51] Roache, P. J. "Perspective: A Method for Uniform Reporting of Grid Refinement Studies." *Journal of Turbomachinery* Vol. 116 No. 3 (1994): pp. 405–413.

[52] Cadence. *Fine Turbo 2024.1 Theory Guide* (2024).

[53] Menter, F. R., Langtry, R. B., Likki, S. R., Suzen, Y. B., Huang, P. G. and Völker, S. "A Correlation-Based Transition Model Using Local Variables—Part I: Model Formulation." *Journal of Turbomachinery* Vol. 128 No. 3 (2004): pp. 413–422.

[54] Sala, Carola Rovira, Dygutsch, Thomas, Frey, Christian, Schnell, Rainer and Martinez Luque, Raul. "Goals and

strategies for open fan design." *International Journal of Turbomachinery, Propulsion and Power* Vol. 10 No. 3 (2025): p. 28.

[55] Drela, Mark. "Power balance in aerodynamic flows." *AIAA Journal* Vol. 47 No. 7 (2009): pp. 1761–1771.

[56] Schnell, Rainer and Mennicken, Maximilian. "Unified Assessment of Open and Ducted Propulsors." *Aerospace* Vol. 11 No. 12 (2024): p. 1002.

[57] Siddappaji, Kiran. "On the entropy rise in general unducted rotors using momentum, vorticity and energy transport." Ph.D. Thesis, University of Cincinnati. 2018. Ch. 2.6.2.